Particle Accelerators, 1985, Vol. 18, pp. 73–99
0031-2460/85/1802–0073/$25.00/0

STUDIES OF A RAPID ELECTRON BEAM ACCELERATOR† (REBATRON)

C. A. KAPETANAKOS, P. SPRANGLE, S. J. MARSH‡, D. DIALETIS and C. AGRITELLIS§

Advanced Accelerator Program, Plasma Physics Division, Naval Research Laboratory, Washington, D.C. 20375

and

A. PRAKASH

Ballistic Research Laboratory, Aberdeen, MD 21005

(Received February 18, 1985; in final form May 17, 1985)

We have carried out an extensive numerical and analytical investigation of the beam dynamics in a rebatron accelerator. In this device acceleration occurs by a localized high-gradient electric field and beam confinement is achieved by a strong-focusing torsatron magnetic field and a vertical magnetic field. In a rebatron, beam acceleration occurs in a few microseconds and limitations imposed by instabilities, field errors and radiation losses can be relaxed. When the vertical magnetic field is independent of time, our studies indicate that both the bandwidth and the maximum electron beam current that can be confined by these devices is remarkably high.

I. INTRODUCTION

Ultra-high current accelerators are rapidly becoming an active area of research.[1,2] The development of these devices is mainly motivated by a variety of potential applications[1,3,4] that are extended over several areas, including environment, food processing, radiation sources, x-ray radiography and national defense.

Among the various accelerating schemes that have the potential to produce ultra-high power electron beams, induction accelerators[1,2] appear to be the most promising. Induction accelerators are inherently low-impedance devices and thus are ideally suited to drive high-current beams. The acceleration process is based on the inductive electric field produced by a time-varying magnetic field.

Quite naturally, induction accelerators are divided into linear[5–13] and cyclic[14–19] devices. In linear devices, the accelerating field is localized in the gap, while in their cyclic counterparts the electric field is continuous along the orbit of the accelerated particles. Both cyclic and linear devices require the same total magnetic-flux change to achieve a given energy increment. However, in linear

† Work jointly supported by the Office of Naval Research and U.S. Army Ballistic Research Laboratory, Aberdeen, Md.

‡ Permanent Address: Sachs/Freeman Associates, Bowie, Md. 20715.

§ Permanent Address: Science Applications. Inc., McLean, Va. 22102.

accelerators the total change of flux occurs in one transit time, typically in less than 100 nsec, while in cyclic accelerators the same change occurs over several thousand revolutions in a typical time of one msec.

As a consequence of the slow acceleration, the accelerated beam must be confined by the focusing magnetic field over long periods of time and thus field errors, instabilities and radiation losses impose limitations on the cyclic accelerators. These limitations can be substantially relaxed if the acceleration could occur rapidly, as in linear accelerators. Therefore, a device that combines the rapid acceleration of linear accelerators and the compact size of cyclic accelerators is highly desirable. In this paper, we propose such a hybrid scheme that combines most of the advantages of linear and cyclic accelerators. This device has been named REBATRON (Rapid Electron Beam Accelerator).

A rebatron is shown schematically in Fig. 1. The high-gradient localized field that is responsible for the rapid acceleration is produced by a convoluted parallel transmission line, although other transmission lines may be more appropriate in an actual system. Since the acceleration occurs over a few μsec, the constraints imposed on the vertical field are very stringent. To reduce the inductance of the system, the vertical field is generated by two coaxial cylindrical plates as shown in the lower right corner of Fig. 1. The axes of these lines coincide with the major axis of the toroidal vessel and they are located symmetrically around the minor

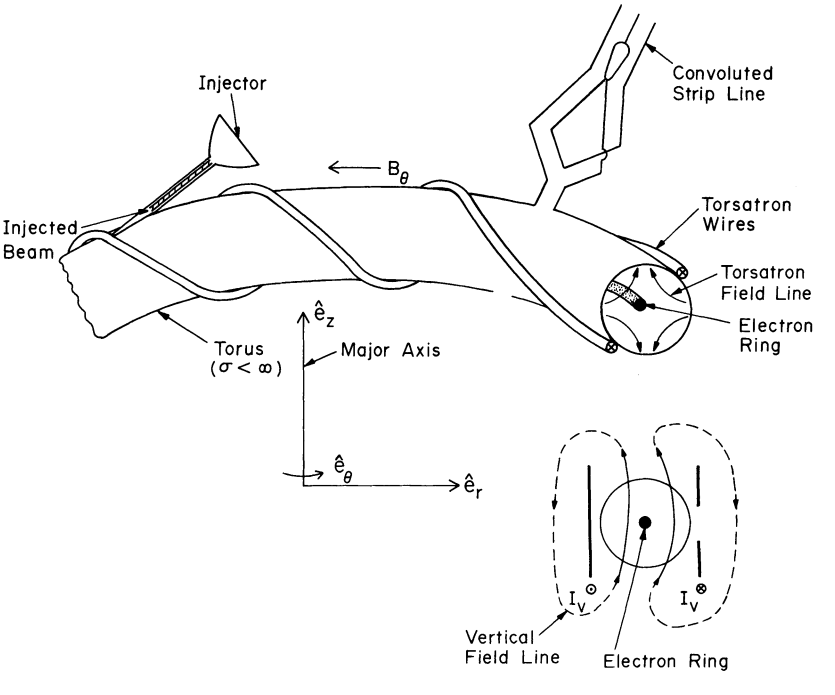

FIGURE 1 Schematic of a rebatron. The accelerating gap is energized by two or more transmission lines that are symmetrically distributed around the minor axis.

axis of the torus. The purpose of the gap in the outer plate is to provide a field with the desirable external field index. The transmission lines change mainly the local vertical magnetic field, while the magnetic flux through the beam orbit remains approximately constant.

The mismatch between the beam energy and the vertical field is alleviated by a strong focusing field. This field is generated by a set of $l = 2$ torsatron windings, i.e., two twisted wires that carry current in the same direction. In addition to the transverse components of the field, the torsatron windings provide a zero-order toroidal magnetic field. The beneficial effect of twisted quadrupole fields on the beam orbits has been recognized for several years.[20] In recent years, the $l = 2$ stellarator field has been used by Roberson *et al.* to improve the bandwidth of the modified betatron in a device named the Stellatron[19] and also in the racetrack accelerator,[21] a device similar to the rebatron.

In addition to alleviating the energy mismatch problem, the strong focusing substantially improves the current-carrying capabilities of the device, in particular at low γ. Our studies show that the maximum electron-beam current that can be confined in a rebatron can be very high. Therefore, it is expected that the limiting current in a rebatron would be determined from collective instabilities and not from the macroscopic stability of the beam orbits.

Beam capture in the rebatron, as in other devices that use strong focusing fields, is very difficult. The reason is that the strong focusing fields make the particle orbits insensitive to the energy mismatch and thus, small changes in the vertical magnetic field are not sufficient to move the beam from the injection position near the wall to the minor axis of the torus. Recently, we have developed two injection schemes that appear very promising. One is based on the drag force of a resistive chamber wall[22] and the other on the modification of the beam orbit by a time-varying magnetic field.

During acceleration, when the vertical magnetic field B_v exceeds by far the torsatron field B_t, the beam dynamics is solely determined by the vertical and toroidal fields. For most applications of interest $B_v \gg B_t$ at the peak of acceleration and thus, beam extraction from the rebatron is similar to that from a modified betatron.[18] There are several extraction schemes presently under investigation at various levels of development. In the conceptually simplest of these schemes, near the end of the acceleration, the vertical field increases slower than its matching value and the beam centroid moves outwards, until it reaches a region where the external field index $n = 0$. In such a region, the electron ring is not confined and thus drifts vertically out of the system. As the vertically drifting ring leaves the torus, it enters a local null-field region and unwinds to a straight beam.

In this report, we present results from our studies of the beam dynamics in a rebatron accelerator when the magnetic fields are not a function of time. In addition, the local vertical magnetic field has been replaced by a time-independent betatron magnetic field. Our results indicate that for realistic values of the fields, the bandwidth of a rebatron can be in excess of 1000%. Results with the local rapidly varying vertical field will be reported in a forthcoming publication.

II. THE APPLIED FIELDS

a. Magnetic Fields

In the local cylindrical coordinate system $\hat{e}_\rho$, $\hat{e}_\phi$, e_s shown in Fig. 2, the magnetic-field components of the $l=2$ torsatron are given by

$$B_\rho = B_\rho^{(0)} + B_{\rho+}^{(1)} + B_{\rho-}^{(1)}, \tag{1a}$$

$$B_\phi = B_\phi^{(0)} + B_{\phi+}^{(1)} + B_{\phi-}^{(1)}, \tag{1b}$$

$$B_s = \frac{1}{1+(\rho/r_0)\cos\phi}[B_s^{(0)} + B_{s+}^{(1)} + B_{s-}^{(1)}], \tag{1c}$$

where

$$B_\rho^{(0)} = B_0 \sum_{m=1}^{\infty} A_m^{(0)} m x_0 I'_{2m}(mx) \sin[2m(\phi - \alpha s)], \tag{2a}$$

$$B_\phi^{(0)} = B_0 \sum_{m=1}^{\infty} A_m^{(0)} 2m \frac{x_0}{x} I_{2m}(mx) \cos[2m(\phi - \alpha s)], \tag{2b}$$

$$B_s^{(0)} = B_0 \left\{ 1 - \sum_{m=1}^{\infty} A_m^{(0)} m x_0 I_{2m}(mx) \cos[2m(\phi - \alpha s)] \right\}, \tag{2c}$$

and[25]

$$B_{\rho\pm}^{(1)} = \frac{1}{4}\frac{\rho_0}{r_0} B_0 \sum_{m=1}^{\infty} \{A_m^{(1)} I'_{2m\pm1}(mx) - A_m^{(0)}[2(1\pm m) mx I'_{2m}(mx) + [(mx)^2 + 2m(2m\pm1)+1] I_{2m}(mx)]\} \sin[(2m\pm1)\phi - 2m\alpha s], \tag{3a}$$

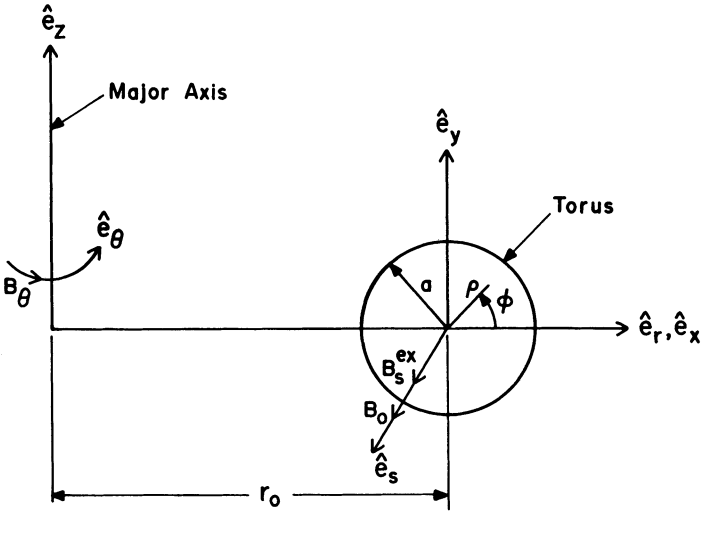

FIGURE 2 Systems of coordinates.

$$B_{\phi\pm}^{(1)} = \frac{1}{4}\frac{\rho_0}{r_0} B_0 \sum_{m=1}^{\infty} (2m \pm 1)\left\{A_m^{(1)} \frac{1}{mx} I_{2m\pm1}(mx) - A_m^{(0)}[mxI'_{2m}(mx) + (1 \pm 2m) I_{2m}(mx)]\right\} \cos[(2m \pm 1)\phi - 2m\alpha s], \quad (3b)$$

$$B_{s\pm}^{(1)} = -\frac{1}{4}\frac{\rho_0}{r_0} B_0 \sum_{m=1}^{\infty} \{A^{(1)} I_{2m\pm1}(mx) - A_m^{(0)} mx[mxI'_{2m}(mx) + (1 \pm 2m) I_{2m}(mx)]\} \cos[(2m \pm 1)\phi - 2m\alpha s]. \quad (3c)$$

The coefficients $A_m^{(0)}$, $A_m^{(1)}$ and C_m are given by the expressions

$$A_m^{(0)} = K'_{2m}(mx_0) C_m, \quad (4a)$$

$$A_m^{(1)} = [(mx_0)^2 K'_{2m}(mx_0) - K_{2m\pm1}(mx_0) + (1 \pm 4m) mx_0 K'_{2m\pm1}(mx_0)] C_m, \quad (4b)$$

$$C_m = \frac{2 \sin 2m\delta}{2m\delta}. \quad (4c)$$

The remaining parameters are defined as follows:

$$B_0 = \frac{8\pi I}{cL}, \quad (5)$$

$$x_0 = 2\alpha\rho_0, \quad (6a)$$

$$x = 2\alpha\rho, \quad (6b)$$

$$\alpha = \frac{2\pi}{L}, \quad (7)$$

where I is the current flowing in the windings, $2\delta\rho_0$ is the width of the current-carrying conductor, ρ_0 is the radius and L is the period of the windings, r_0 is the major radius of the torus, B_s^{ex} is the external toroidal magnetic field and $I_n(x)$, $K_n(x)$, $I'_n(x)$ and $K'_n(x)$ are the Bessel functions and their derivatives. In a toroidal device, the period should satisfy the relation

$$\frac{2\pi r_0}{L} = N, \quad (8)$$

where N is an integer. The zero-order fields $B_\rho^{(0)}$, $B_\phi^{(0)}$ and $B_s^{(0)}$ are the field components produced by the helical windings in a straight (cylindrical) configuration[23,24] and the terms proportional to ρ_0/r_0 are the first-order toroidal corrections. These corrections, as given in Eqs. (3), have been obtained for the surface current density

$$J_\rho = 0, \qquad J_\phi = \left(\frac{I}{2\delta\rho_0}\right)\left[\frac{\alpha\rho_0}{1 + (\rho_0/r_0)\cos\phi}\right] f(\phi - \alpha s) \quad \text{and} \quad J_s = \frac{I}{2\delta\rho_0} f(\phi - \alpha s),$$

where $f(\phi)$ is a periodic function of ϕ with period π, and

$$f(\phi) = \begin{cases} 1, & \text{for} \quad -\gamma < \phi < \gamma \\ 0, & \gamma < \phi < \pi - \gamma. \end{cases}$$

The three magnetic field components for $s = 0$ are plotted in Figs. 3a and 3b for $\phi = 0$ and $\phi = \pi/2$ respectively. The various parameters for these plots are listed in Table I. At $\phi = 0$, the radial component of the field is zero. The B_ϕ component increases linearly with ρ near the minor axis and considerably faster near the wires. The toroidal correction at $\rho = 0$ is approximately -36 G. In the results

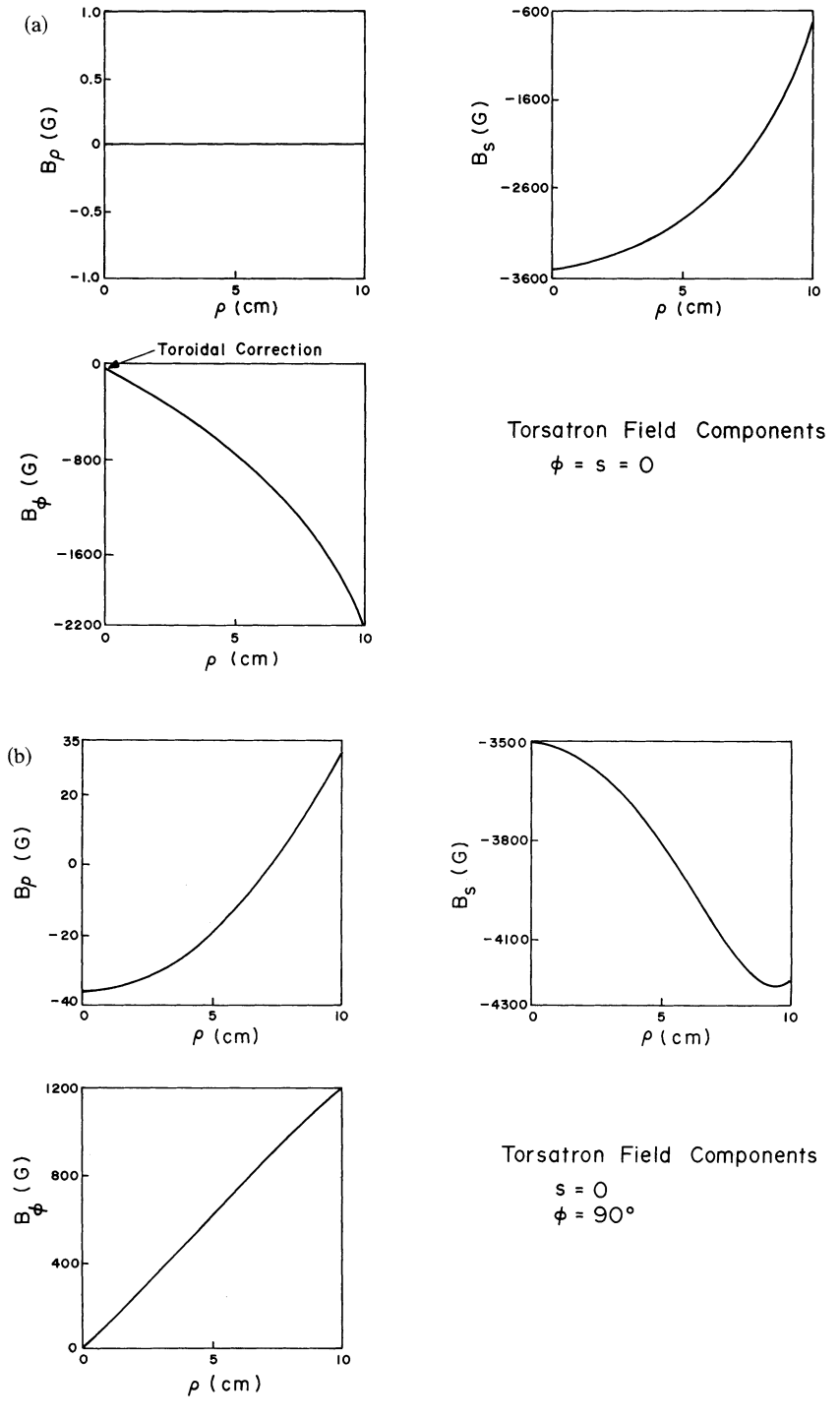

FIGURE 3 Torsatron magnetic field components (a) at $\phi = s = 0$ and (b) at $s = 0$, $\phi = \pi/2$. In addition to the torsatron field there is toroidal field $B_s^{ex} = -6$ kG that is produced by a set of toroidal coils. (c) magnetic field lines in r, z and ρ, s planes.

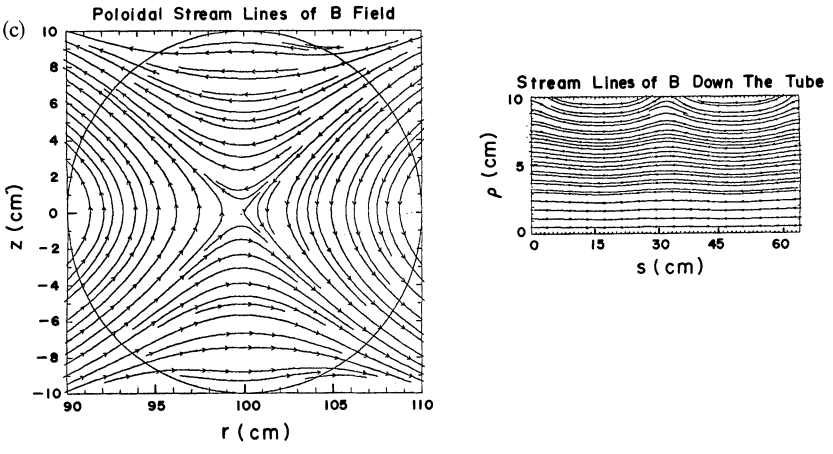

FIGURE 3 (*cont'd*)

shown in Fig. 3, in addition to the toroidal field produced by the torsatron windings, there is a −6 kG field produced by a set of toroidal coils. At $\rho = 0$, $B_s = B_s^{ex} + B_0 = -6 + 2.5 = -3.5$ kG. It is apparent from these results that the toroidal field B_s does not vary as $1/r$. The reason is that B_s is a function of s or the toroidal angle. Figure 3c gives the magnetic field lines in the r, z and ρ, s planes. Because of the toroidal corrections, the magnetic axis does not coincide with the minor axis of the torus, which is located at $r = 100$ cm. The magnetic axis is always shifted toward the major axis of the torus, because the field on the minor axis generated by the axial current flowing on the section of the torus to the left of the major axis reinforces the field generated by the axial current flowing in the outside edge of the torus that is located to the right of the major axis.

Equations (1) to (7) are used to compute the magnetic-field components in the numerical integration of the orbit equations. It has been determined that the first two non-zero terms in the expansion are sufficient to describe the field in the region $\rho/a \leqslant 0.5$ with an accuracy better than 95%.

In the analytical work described in Section IV, the toroidal corrections have been neglected as well as all the terms with $m \geqslant 2$. Furthermore, it has been assumed that $\delta \ll 1$. Under these simplifications the torsatron magnetic field

TABLE I

Parameters relevant to the torsatron fields shown in Fig. 3. Only two terms retained in the series of Eqs. (1) to (3)

Torus major radius r_0 (cm)	= 100
Windings minor radius ρ_0 (cm)	= 12
Toroidal chamber minor radius a (cm)	= 10
$\alpha = 2\pi/L$ (cm^{-1})	= 0.1
Field strength factor ε_t	= 0.2
Winding current I(kA)	= 62.37
l	= 2
Additional toroidal field B_s^{ex} (kG)	= −6

becomes

$$B_\rho \simeq 2B_s^{ex}\varepsilon_t I_2'(x)\sin[2(\phi-\alpha s)], \tag{9}$$

$$B_\phi \simeq \frac{4B_s^{ex}}{x}\varepsilon_t I_2(x)\cos[2(\phi-\alpha s)], \tag{10}$$

$$B_s \simeq B_0 - 2B_s^{ex}\varepsilon_t I_2(x)\cos[2(\phi-\alpha s)], \tag{11}$$

where $B_s^{ex}\varepsilon_t = B_0 x_0 K_2'(x_0)$. For $x \ll 1$, Eqs. (9), (10) and (11) become

$$B_\rho \simeq \frac{B_s^{ex}\varepsilon_t x}{2}\sin[2(\phi-\alpha s)], \tag{12}$$

$$B_\phi \simeq \frac{B_s^{ex}\varepsilon_t x}{2}\cos[2(\phi-\alpha s)], \tag{13}$$

$$B_s \simeq B_0. \tag{14}$$

In addition to the torsatron field, the rebatron accelerator includes a betatron or vertical magnetic field and a toroidal field, B_s^{ex}, that is produced by a set of toroidal coils. The two components of the betatron field are described by the linearized equations

$$B_z \simeq B_{z0}[1 - n(r-r_0)/r_0], \tag{15}$$

$$B_r \simeq -B_{z0}nz/r_0, \tag{16}$$

where B_{z0} is the betatron field at the reference orbit, i.e., at $x = y = 0$ and n is the external field index.

The toroidal field produced by a set of toroidal coils is independent of the toroidal angle and therefore varies as $1/r$. This toroidal field can be chosen to have either the same or opposite polarity to the torsatron toroidal field.

b. The Electric Field in the Gap

Consider two cylinders with their axes lying along the same line and separated by a distance d, as shown in Fig. 4a. Since the cylinder on the left is charged to $-V_0$ and the cylinder to the right is charged to $+V_0$ the average electric field in the gap is $\langle E_s\rangle = 2V_0/d$. The local electric field is given by the solution of Laplace's equation, i.e., $\nabla^2\Phi = 0$. For $|s| \geq d/2$, the exact components of the electric field are

$$E_s = -\frac{4V_0}{d}\sum_{n=1}^{\infty}\frac{\sinh(\lambda_n d/2)J_0(\lambda_n\rho)e^{-\lambda_n|s|}}{\lambda_n a J_1(\lambda_n a)}, \tag{17}$$

$$E_\rho = -\frac{s}{|s|}\frac{4V_0}{d}\sum_{n=1}^{\infty}\frac{\sinh(\lambda_n d/2)J_1(\lambda_n\rho)e^{-\lambda_n|s|}}{\lambda_n a J_1(\lambda_n a)}. \tag{18}$$

Similarly, for $|s| \leq d/2$, the two components of the electric field are

$$E_s = -\frac{4V_0}{d}\left[\frac{1}{2} - \sum_{n=1}^{\infty}\frac{J_0(\lambda_n)e^{-\lambda_n d/2}\cosh(\lambda_n s)}{a\lambda_n J_1(\lambda_n a)}\right], \tag{19}$$

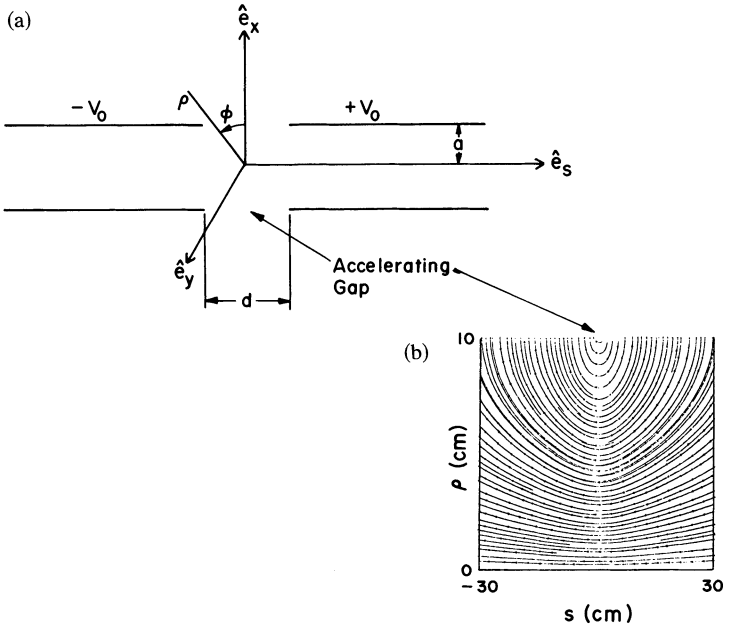

FIGURE 4 (a) configuration and (b) field lines of the accelerating electric field.

and

$$E_\rho = -\frac{4V_0}{d}\sum_{n=1}^{\infty}\frac{J_1(\lambda_n\rho)e^{-\lambda_n d/2}\sinh(\lambda_n s)}{\lambda_n a J_1(\lambda_n a)}, \tag{20}$$

where $J_0(\lambda_n a)=0$, a is the radius of the cylinders and J_0 and J_1 are Bessel functions.

The electric-field lines that correspond to the field components given by Eqs. (17) to (20) are plotted in Fig. 4b. These electric fields are a good representation of the fields produced inside the torus by a transmission line, since in this region the inductive magnetic field is zero and therefore the potential is described by $\nabla^2\varphi=0$.

III. NUMERICAL RESULTS

To investigate the confining properties of the torsatron magnetic field, we have integrated the relativistic equations of motion using Eqs. (1) to (7) for the torsatron magnetic field and Eqs. (15) and (16) for the betatron field. The accelerating gap is 2 cm wide and, as shown in Fig. 5, the electric field is limited to a 0.60-radian wide toroidal sector. For reasons that are discussed later on, the self fields have been omitted in these runs.

In the first run, the current in the torsatron windings is chosen to be zero. Figure 6a shows the normalized particle energy (γ) as a function of time and Fig.

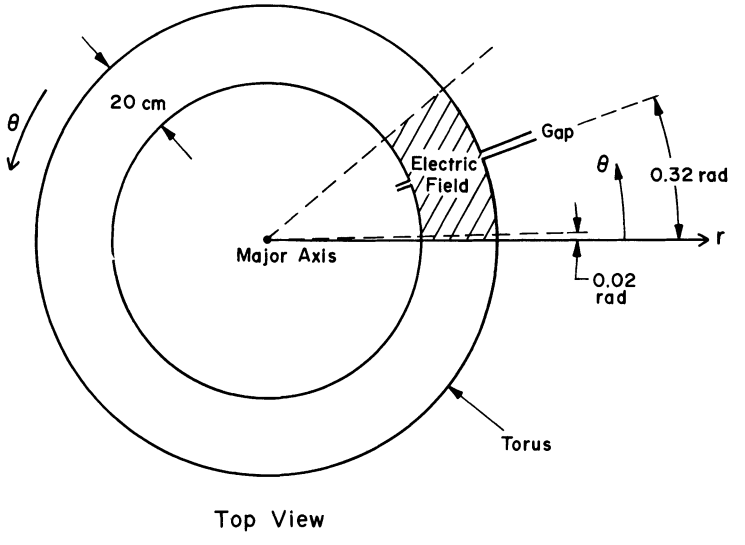

FIGURE 5 Top view of the torus. The accelerating field is limited to ±30 cm around the gap.

6b the projection of the particle orbit in the transverse plane. The various parameters for this run are listed in Table II. Since ε_t is zero, the magnetic field configuration is that of the modified betatron. As a consequence of the curvature drift, the gyrating particle drifts out of the system in about 26 nsec, i.e., in about a revolution around the major axis. As expected, the guiding center of the particle moves mainly in the vertical direction, while the particle gyrates around its guiding center with a frequency corresponding to the local toroidal field.

Figures 7a and 7b show the normalized energy of the particle and its orbit when approximately −124.7 kA of current flows through the torsatron windings. The rest of the parameters for this run are listed in Table III. The particle remains confined for eight revolutions. Figures 8a and 8b show similar results when the current in the windings is increased to approximately −250 kA. The corresponding torsatron field-strength factor ε_t is −0.8. The remainder of the parameters are listed in Table IV. In all three runs the betatron magnetic field was held constant at 118 G. These results clearly demonstrate that the confining properties of the system are substantially improved by the addition of the torsatron field. The particle strikes the chamber wall when its γ approaches approximately 65. The total time the particle remains in the system is about 320 nsec, i.e., more than an order of magnitude longer than when the torsatron field is absent.

Further improvement in the particle confinement is observed when the period of the windings is reduced or the current in the windings increased. An additional modest improvement in the confinement of the system is observed when the betatron field is increased above its matching value. This is shown in Fig. 9. The betatron field for this run is 236 G and the remainder of the parameters are identical to those in Fig. 8. The confinement time increased by 20 nsec, i.e., from 320 to 340 nsec. However, when the betatron field increased to 472 G, the confinement time was reduced to 290 nsec.

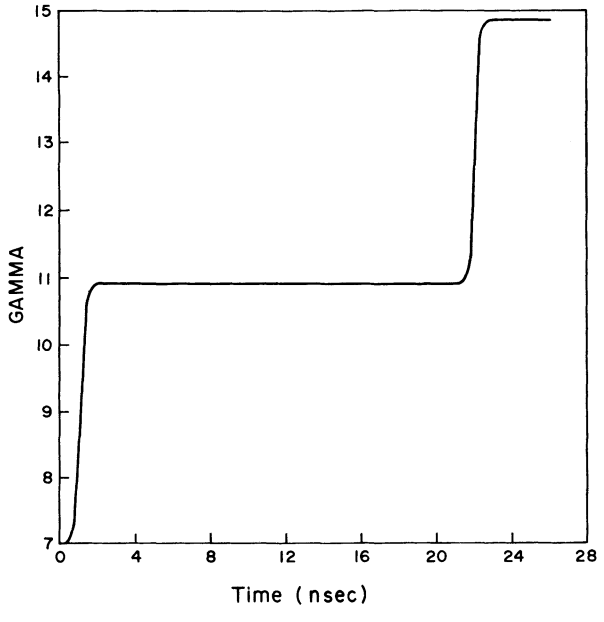

(a)

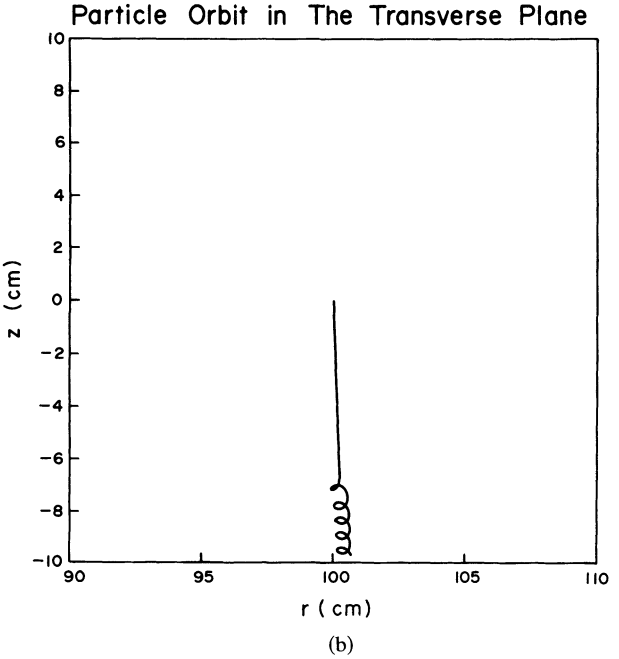

(b)

FIGURE 6 (a) γ of particle as a function of time and (b) particle orbit in the r, z plane in the absence ($\varepsilon_t = 0$) of torsatron field. The various parameters for this run are listed in Table II.

TABLE II

Parameters of the run shown in Fig. 6

Torus major radius r_0 (cm)	= 100
Winding minor radius ρ_0 (cm)	= 12
Toroidal chamber minor radius a (cm)	= 10
$\alpha = 2\pi/L$ (cm^{-1})	= 0.1
Field strength factor ε_t	= 0
Winding current I (kA)	= 0
l	= 2
Additional toroidal field B_s^{ex} (kG)	= −6
Betatron field B_{z0} (G)	= 118
Ext. field index n	= 0.5
Initial γ	= 7.0
Initial positions $\rho = \phi = s$	= 0
Initial velocities $v_\rho = v_\phi = 0, \quad v_s \approx c$	

IV. THEORETICAL MODEL

To gain a better understanding of the focusing properties of the torsatron fields, we have developed a theoretical model that is based on linear external fields. Obviously, these fields are appropriate only near the minor axis of the torus, i.e., when $2\alpha\rho \ll 1$.

The components of the torsatron field in the coordinate system $\hat{e}_r$, $\hat{e}_\theta$, $\hat{e}_z$ shown

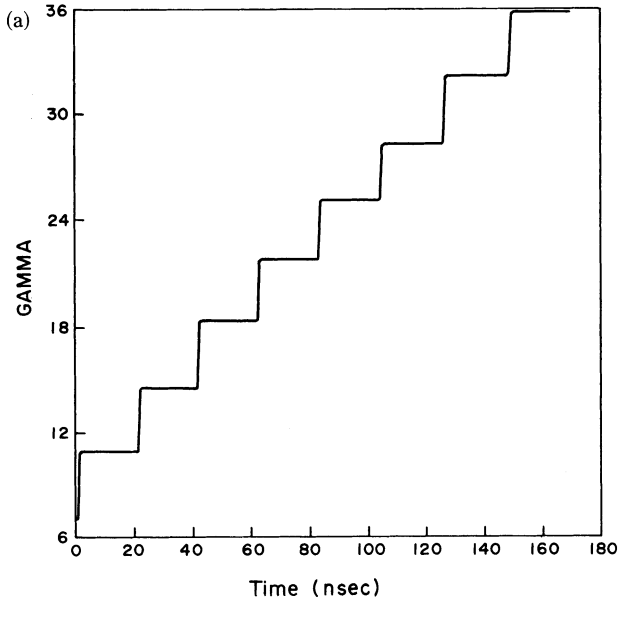

FIGURE 7 (a) γ of particle as a function of time and (b) particle orbit in the r, z plane for moderate ($\varepsilon_t = -0.4$) torsatron field. The various parameters for this run are listed in Table III.

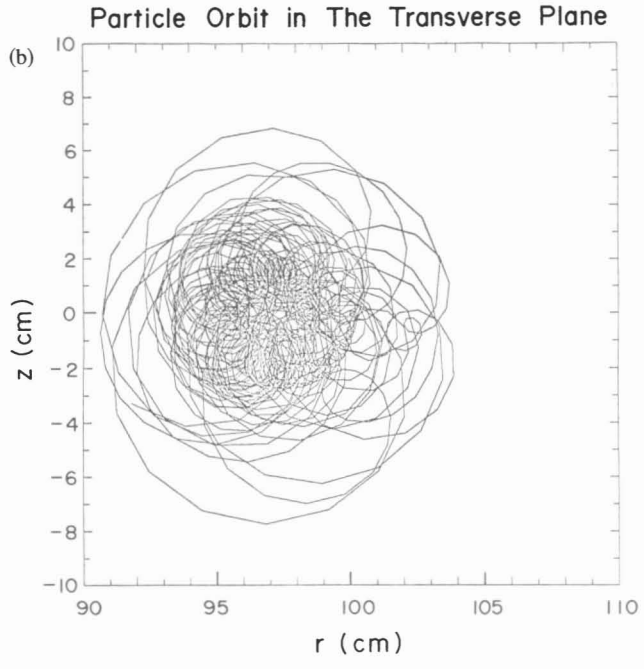

FIGURE 7 (*cont'd*)

in Fig. 2 are

$$B_{rt} = B_\rho \cos\phi - B_\phi \sin\phi = B_s^{ex}\varepsilon_t\alpha[z\cos 2\alpha r_0\theta + (r-r_0)\sin 2\alpha r_0\theta], \quad (21)$$

$$N_{zt} = B_\rho \sin\phi + B_\phi \cos\phi = B_s^{ex}\varepsilon_t\alpha[(r-r_0)\cos 2\alpha r_0\theta - z\sin 2\alpha r_0\theta], \quad (22)$$

$$B_{\theta t} = -B_0, \quad (23)$$

where $-r_0\theta = s$.

TABLE III

Parameters of the run shown in Fig. 7

Torus major radius r_0 (cm)	$= 100$
Winding minor radius ρ_0 (cm)	$= 12$
Toroidal chamber minor radius a (cm)	$= 10$
$\alpha = 2\pi/L$ (cm^{-1})	$= 0.1$
Field strength factor ε_t	$= -0.4$
Winding current I (kA)	$= -124.7$
l	$= 2$
Additional toroidal field B_s^{ex} (kG)	$= -6$
Betatron field B_{z0} (G)	$= 118$
Ext. field index n	$= 0.5$
Initial γ	$= 7.0$
Initial positions $\rho = \phi = s$	$= 0$
Initial velocities $v_\rho = v_\phi = 0, \quad v_s \approx c$	

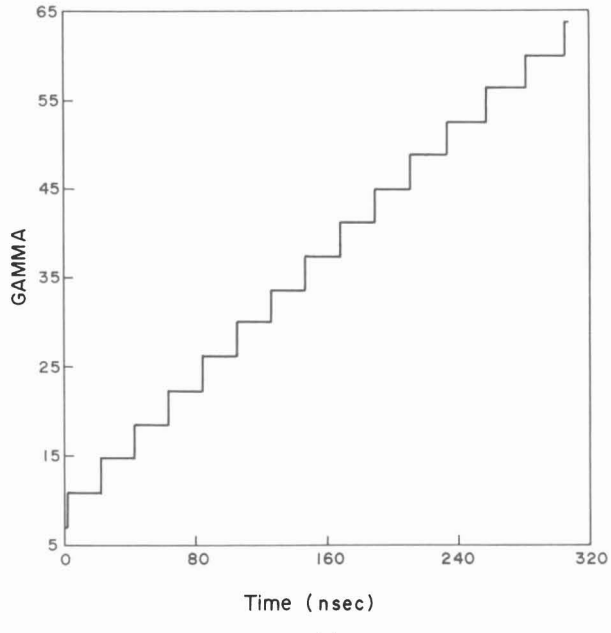

(a)

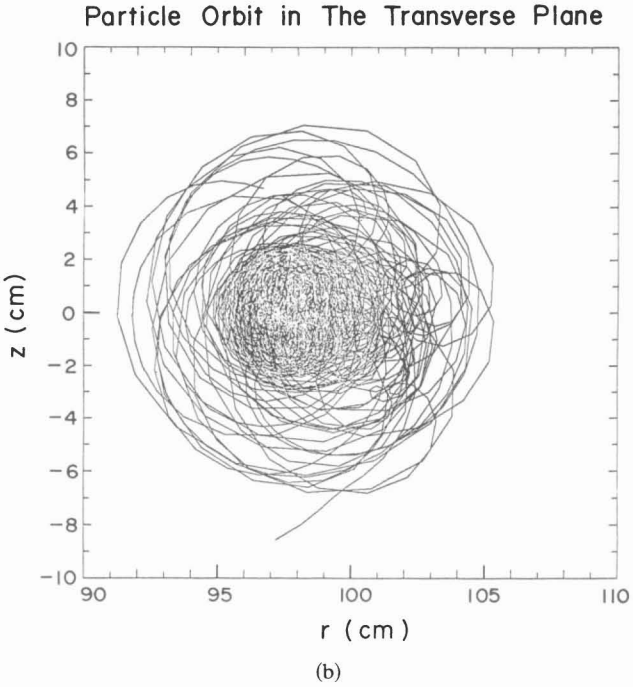

(b)

FIGURE 8 (a) γ of particle as a function of time and (b) particle orbit in the r, z plane for high ($\varepsilon_t = -0.8$) torsatron field. The various parameters for this run are listed in Table IV.

TABLE IV

Parameters of the run shown in Fig. 8

Torus major radius r_0 (cm)	= 100
Winding minor radius ρ_0 (cm)	= 12
Toroidal chamber minor radius a (cm)	= 10
$\alpha = 2\pi/L$ (cm^{-1})	= 0.1
Field strength factor ε_t	= −0.8
Winding current I (kA)	= −250
l	= 2
Additional toroidal field B_s^{ex} (kG)	= −6
Betatron field B_{z0} (G)	= 118
Ext. field index n	= 0.5
Initial γ	= 7.0
Initial positions $\rho = \phi = s$	= 0
Initial velocities $v_\rho = v_\phi = 0, \quad v_s \approx c$	

In addition, the betatron magnetic field is given by

$$B_{zb} \simeq B_{z0}\left[1 - \frac{n(r-r_0)}{r_0}\right], \tag{24}$$

and

$$B_{rb} \simeq -nB_{z0}z/r_0, \tag{25}$$

where n is the external field index. The total field components are

$$B_r = B_{rt} + B_{rb}, \tag{26}$$

$$B_z = B_{zt} + B_{zb}, \tag{27}$$

$$B_\theta = B_{\theta t} - B_s^{ex}, \tag{28}$$

where B_s^{ex} indicates any additional toroidal field that may be applied.

The accelerating electric-field components are approximated by

$$E_r \simeq \frac{(r-r_0)}{2r_0}\ddot{\gamma}\left(\frac{mc^2}{e}\frac{r_0}{v_\theta^2}\right), \tag{29}$$

$$E_z \simeq \frac{z}{2r_0}\ddot{\gamma}\left(\frac{mc^2}{e}\frac{r_0}{v_\theta^2}\right), \tag{30}$$

$$E_\theta \simeq -\frac{mc^2}{ev_\theta}\dot{\gamma}, \tag{31}$$

where $\dot{\gamma} = d\gamma/dt$, $\ddot{\gamma} = d^2\gamma/dt^2$ and v_θ is the toroidal velocity, which is assumed constant.

Using Eqs. (26) to (31) for the fields, the equations of motion in the laboratory frame become

$$\ddot{R} + \omega_R^2 R + \frac{\omega_0\omega_w}{2}[R\cos\omega_w t - Z\sin\omega_w t) - \left(\dot{Z} - \frac{\dot{\gamma}}{2\gamma}Z\right)\frac{\Omega_\theta}{\gamma} = \lambda^2(t), \tag{32}$$

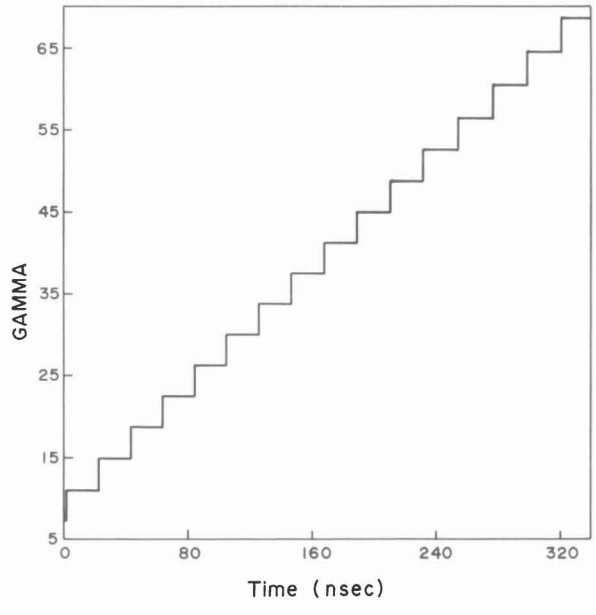

(a)

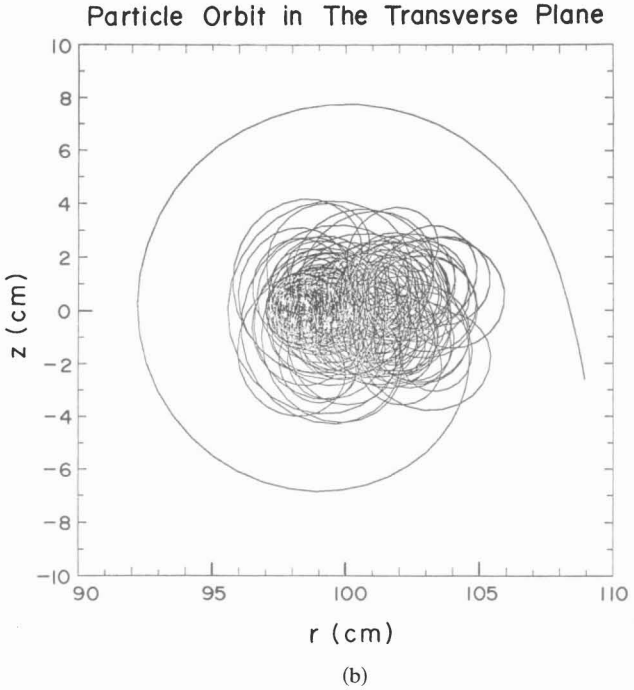

(b)

FIGURE 9 (a) γ of particle as a function of time and (b) particle orbit in the r, z plane for the same parameters as Fig. 8 except at a higher betatron field.

$$\ddot{Z}+\omega_z^2 Z-\frac{\omega_0\omega_w}{2}(Z\cos\omega_w t+R\sin\omega_w t)+\left(\dot{R}-\frac{\dot{\gamma}}{2\gamma}R\right)\frac{\Omega_\theta}{\gamma}=0, \tag{33}$$

where

$$R=\gamma^{1/2}(r-r_0), \qquad Z=\gamma^{1/2}z,$$

$$\Omega_\theta=eB_\theta/mc, \qquad \Omega_{z0}=eB_{z0}/mc, \qquad \omega_0=\Omega_s^{ex}\varepsilon_t/\gamma, \qquad \omega_w=2\alpha v_\theta,$$

$$\lambda^2(t)=\frac{c^2}{r_0}\gamma^{1/2}\frac{v_\theta}{c}\left(\frac{v_\theta}{c}-\frac{r_0\Omega_{z0}}{c\gamma}\right),$$

$$\omega_R^2=\frac{1}{4}\left(\frac{\dot{\gamma}}{\gamma}\right)^2-\frac{1}{2}\left(\frac{\ddot{\gamma}}{\gamma}\right)+\frac{\ddot{\gamma}}{\gamma}\left(\frac{c^2}{2v_\theta^2}\right)-\frac{v_\theta\Omega_{z0}}{\gamma}\frac{n}{r_0}+\frac{v_\theta^2}{r_0^2},$$

and

$$\omega_z^2=\frac{1}{4}\left(\frac{\ddot{\gamma}}{\gamma}\right)^2-\frac{1}{2}\left(\frac{\ddot{\gamma}}{\gamma}\right)+\frac{\ddot{\gamma}}{\gamma}\left(\frac{c^2}{2v_\theta^2}\right)+\frac{v_\theta\Omega_{z0}n}{\gamma r_0}.$$

Equations (32) and (33) become more tractable when transformed to a frame rotating with angular frequency $\omega_w/2$. Using the transformation

$$R=\hat{R}\cos\left(\frac{\omega_w t}{2}\right)+\hat{R}\sin\left(\frac{\omega_w t}{2}\right), \tag{34}$$

$$Z=-\hat{R}\sin\left(\frac{\omega_w t}{2}\right)+\hat{Z}\cos\left(\frac{\omega_w t}{2}\right), \tag{35}$$

Eqs. (32) and (33) become

$$\ddot{\hat{R}}+\left[\omega_\perp^2-\delta\omega^2\cos\omega_w t+\frac{\omega_0\omega_w}{2}-\left(\frac{\omega_w}{2}\right)^2+\left(\frac{\omega_w}{2}\right)\frac{\Omega_\theta}{\gamma}\right]\hat{R}$$
$$+\left(\omega_w-\frac{\Omega_\theta}{\gamma}\right)\dot{\hat{Z}}+\left(\frac{\dot{\gamma}}{2\gamma}\frac{\Omega_\theta}{\gamma}-\delta\omega^2\sin\omega_w t\right)\hat{Z}=\lambda^2\cos\left(\frac{\omega_w t}{2}\right), \tag{36}$$

$$\ddot{\hat{Z}}+\left[\omega_\perp^2+\delta\omega^2\cos\omega_w t-\frac{\omega_0\omega_w}{2}-\left(\frac{\omega_w}{2}\right)^2+\left(\frac{\omega_w}{2}\right)\frac{\Omega_\theta}{\gamma}\right]\hat{Z}$$
$$-\left(\omega_w-\frac{\Omega_\theta}{\gamma}\right)\dot{\hat{R}}-\left(\frac{\dot{\gamma}}{2\gamma}\frac{\Omega_\theta}{\gamma}+\delta\omega^2\sin\omega_w t\right)\hat{R}=\lambda^2\sin\left(\frac{\omega_w t}{2}\right), \tag{37}$$

where

$$\omega_\perp^2=\frac{1}{4}\left(\frac{\dot{\gamma}}{\gamma}\right)^2-\frac{1}{2}\left(\frac{\ddot{\gamma}}{\gamma}\right)+\frac{\ddot{\gamma}}{\gamma}\left(\frac{c^2}{2v_\theta^2}\right)+\frac{v_\theta^2}{2r_0^2}\simeq\frac{1}{4}\left(\frac{\dot{\gamma}}{\gamma}\right)^2+\frac{v_\theta^2}{2r_0^2},$$

and

$$\delta\omega^2=\frac{v_\theta n}{r_0}\left(\frac{\Omega_{z0}}{\gamma}-\frac{v_\theta}{2nr_0}\right)$$

when $|\omega_0\omega_w/2|\gg|\delta\omega^2|$, the two coupled equations (36) and (37) can be combined into a single equation by introducing the complex variable $\hat{\psi}=\hat{R}+i\hat{Z}$. Multiplying Eq. (37) by i and adding it to Eq. (36) we obtain

$$\ddot{\hat{\psi}}+f_1\hat{\psi}+f_3\hat{\psi}^*-if_2\dot{\hat{\psi}}=\lambda^2 e^{i\omega_w t/2}, \tag{38}$$

where

$$f_1 = \omega_\perp^2 - \left(\frac{\omega_w}{2}\right)^2 + \frac{\omega_w}{2}\frac{\Omega_\theta}{\gamma} - \frac{i\dot{\gamma}}{2\gamma}\frac{\Omega_\theta}{\gamma}, \qquad f_2 = \omega_w - \frac{\Omega_\theta}{\gamma} \quad \text{and} \quad f_3 = \frac{\omega_0\omega_w}{2}$$

Equations (36) and (37) have been solved numerically. After integration, the orbit is transferred back to the laboratory frame. The results are shown in Fig. 10. The projection of the orbit in the r, z plane is shown in Fig. 10a, the particle radial distance from the minor axis as a function of time is shown in Fig. 10b and γ as a function of time in Fig. 10c. The various parameters for this run are identical to those listed in Table IV. The particle strikes the wall at about 325 nsec, when its gamma is approximately 68. These results are in good agreement with those of Fig. 8 that have been obtained using the more accurate expressions for the torsatron fields. As will be discussed later, the particle was lost because at $\gamma \approx 65$ it entered the unstable region that extends from $\gamma = 65$ to $\gamma = 121$.

When $\dot{\gamma} = 0$, the homogeneous part of Eq. (38) becomes

$$\dddot{\hat{\psi}} + [2f_1 + f_2^2]\ddot{\hat{\psi}} + [f_1^2 - f_3^2]\hat{\psi} = 0, \tag{39}$$

i.e., a fourth-order equation with constant coefficients. The solutions of Eq. (39)

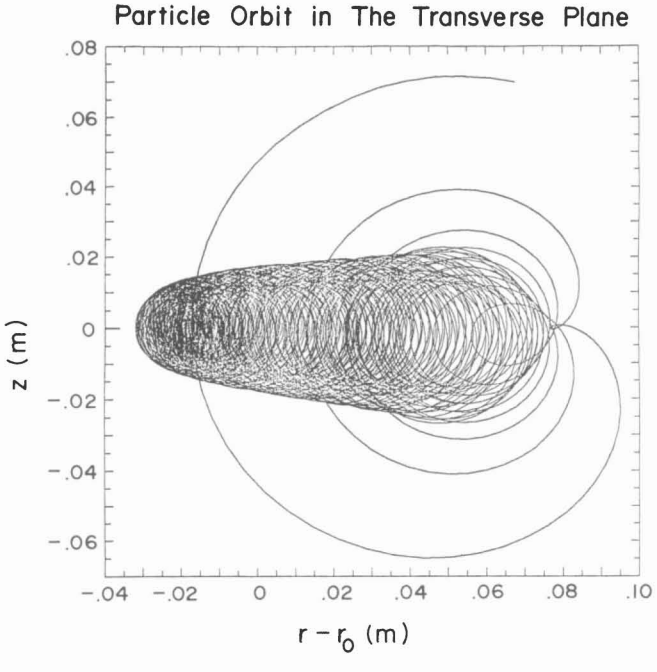

(a)

FIGURE 10 (a) particle orbit in the r, z plane; (b) particle radius as a function of time and (c) γ of particle as a function of time. These results have been obtained from the linear equations (36) and (37). The results shown are in the Lab. frame. The various parameters for this run are the same with those of Fig. 8.

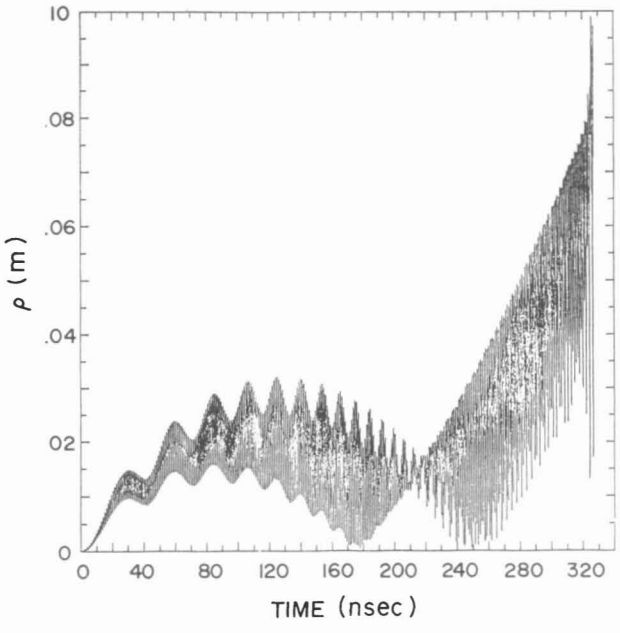

(b)

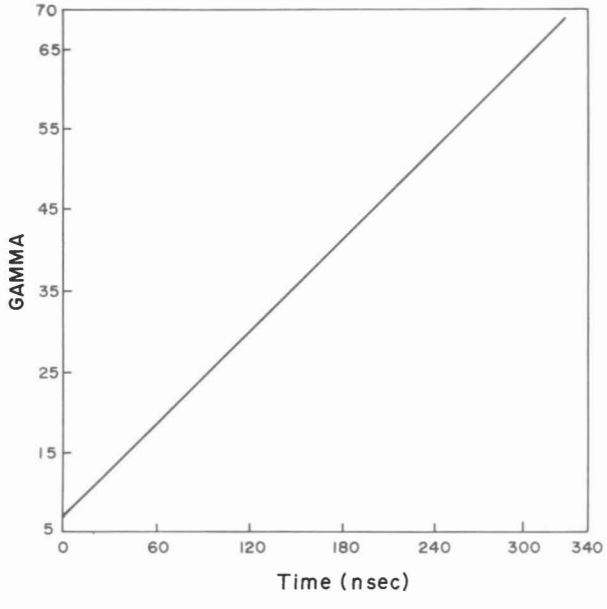

(c)

FIGURE 10 (*cont'd*)

are of the type $\hat{\psi} = \hat{\psi}_0 e^{i\omega t}$, where ω^2, is given by

$$\omega_{\pm}^2 = \frac{1}{4}\left(\omega_w - \frac{\Omega_\theta}{\gamma}\right)^2 + \frac{\Omega_\theta^2}{4\gamma^2} \pm \frac{\Omega_\theta}{2\gamma}\left[\left(\omega_w - \frac{\Omega_\theta}{\gamma}\right)^2 + \omega_w^2 \varepsilon_t^2 \left(\frac{\Omega_s^{ex}}{\Omega_0}\right)^2\right]^{1/2}, \tag{40}$$

when $|\omega_\perp^2| \ll |\omega_0 \omega_w/2|$. The particle orbits are stable when ω is real, i.e., when

$$\mu(\gamma) \equiv \left(\Omega_\theta - \frac{\omega_w \gamma}{2}\right)^2 - \varepsilon_t^2 \Omega_s^{ex2} \geq 0 \tag{41}$$

The two roots of (40) are given by

$$\gamma_{\pm} = \frac{2\Omega_\theta}{\omega_w}\left(1 \pm \varepsilon_t \frac{\Omega_s^{ex}}{\Omega_\theta}\right). \tag{42}$$

The function $\mu(\gamma)$ is plotted in Fig. 11 for three values of B_θ and B_s^{ex}. In Fig. 11a $B_s^{ex} = -6$ kG, $B_0 = 5$ kG and thus $B_\theta = -(B_s^{ex} + B_0) = 1$ kG. For this value of toroidal magnetic field and for $\varepsilon_t = 0.4$ and $\omega_w/2 = 3 \times 10^9\,\text{sec}^{-1}$, Eq. (42) gives 19.96 and -8.2 for the two roots of Eq. (41). Therefore, at $\gamma = 7$ the particle orbit should be unstable. Results from the numerical integration of the nonlinear orbit equations for $\dot{\gamma} = 0$, and $\gamma = 7$ and using the same values for the rest of the parameters as in Fig. 11a are shown in Fig. 12. As expected, the orbit is indeed unstable and the particle is lost in less than one nsec.

By reversing the direction of the current in the torsatron wires, B_0 and ε_t change sign and the two roots of Eq. (41) become 50.5 and 78.7. Therefore for $\gamma = 7$ the orbit is stable. This is in agreement with the results from the numerical integration of nonlinear orbit equations shown in Fig. 13.

When $\gamma_{\pm} < 1$, the orbits are stable for all values of γ. For $B_s^{ex} = 6$ kG. $B_0 = 5$ kG and $\varepsilon_t = -0.4$ the two roots of Eq. (41) are -50.5 and -78. For this case the orbits were found stable for all the values of γ considered.

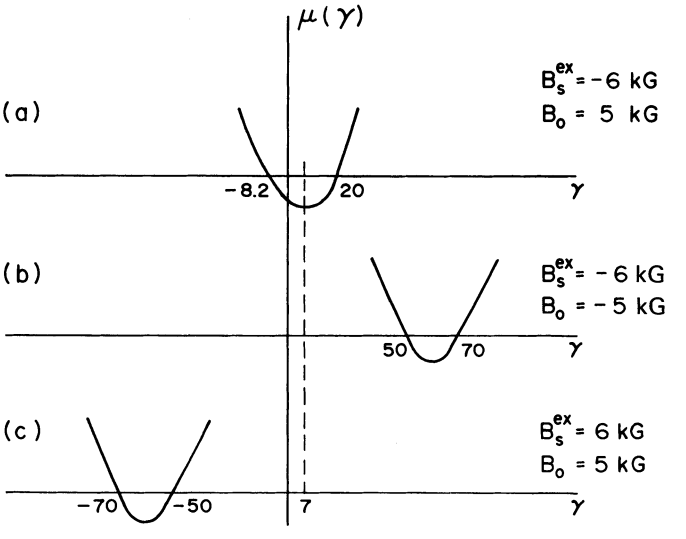

FIGURE 11 Plot of $\mu(\gamma)$ given in Eq. (41) for three different combinations of B_s^{ex} and B_0.

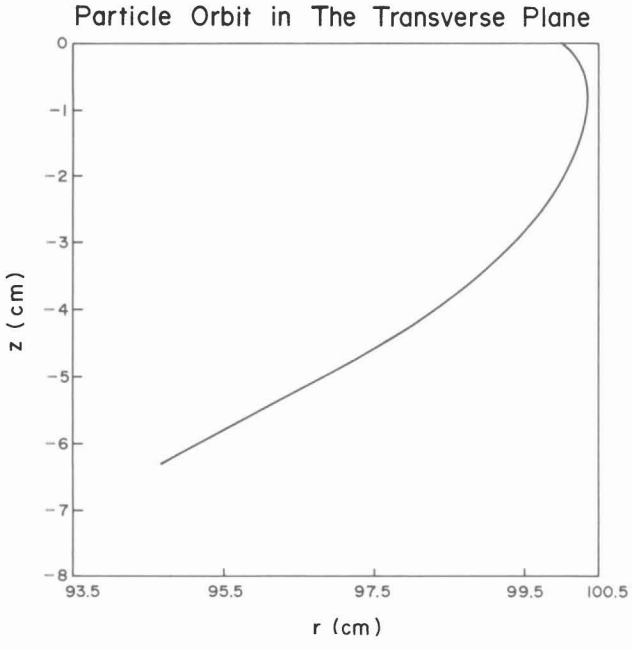

FIGURE 12 Particle orbit in the r, z plane for the same parameters as those of Fig. 11a.

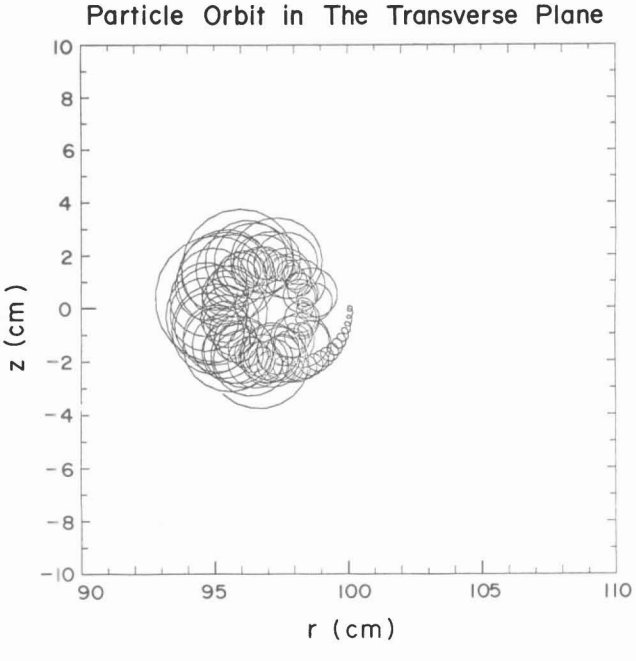

FIGURE 13 Particle orbit in the r, z plane for the same parameters as those of Fig. 11b.

The numerical and theoretical results are in excellent agreement when the linearized theoretical model is valid. However, when B_s^{ex} and B_0 have opposite signs and $|B_s^{ex}| > |B_0|$, the toroidal field vanishes at some radial distance and the field lines form magnetic cusps. In this case, the linear theory does not properly describe the fields and the predictions of the theory are not in agreement with the numerical results.

When

$$\left[\omega_0^2\omega_w^2/\left(\omega_w - \frac{\Omega_\theta}{\gamma}\right)^2\left(\frac{\Omega_\theta^2}{\gamma^2}\right)\right] \ll 1,$$

Equation (40) gives

$$\omega_\pm^2 = \begin{cases} (\omega_w/2)^2\left[1 + \dfrac{\omega_0^2}{(\omega_w - \Omega_\theta/\gamma)(\Omega_\theta/\gamma)}\right], & \text{(slow mode)} \\ -\dfrac{\omega_w^2}{4} + \dfrac{\Omega_\theta^2}{\gamma^2} - \omega_w\dfrac{\Omega_\theta}{\gamma} - \dfrac{\omega_0^2\omega_w^2}{4(\omega_w - \Omega_\theta/\gamma)(\Omega_\theta/\gamma)}. & \text{(fast mode)} \end{cases}$$

In the laboratory frame, the slow mode Ω_+ becomes

$$\Omega_+ = \omega_+ - \frac{\omega_w}{2} = \frac{\omega_0^2}{4\left(1 - \dfrac{\Omega_\theta}{\gamma\omega_w}\right)\left(\dfrac{\Omega_\theta}{\gamma}\right)}. \tag{43}$$

The particular solution of Eq. (38) in the rotating frame, for $\dot{\gamma} = 0$ and $\omega_\perp^2$ small, is $\hat{\Psi}_p = \hat{R}_p + i\hat{Z}_p$, where

$$\hat{R}_p = \frac{4\lambda^2(\omega_w - \Omega_\theta/\gamma + \omega_0/2)}{\omega_0^2\omega_w}\cos\left(\frac{\omega_w t}{2}\right), \tag{44}$$

and

$$\hat{Z}_p = \frac{4\lambda^2(\omega_w - \Omega_\theta/\gamma - \omega_0/2)}{\omega_0^2\omega_w}\sin\left(\frac{\omega_w t}{2}\right). \tag{45}$$

Transforming back to the laboratory frame using the transformation $\psi = \hat{\Psi}e^{-i\omega_w t/2}$, we find that the particle orbit is displaced along the horizontal axis by

$$\Delta r = \frac{4\lambda^2}{\omega_0^2\gamma^{1/2}}(1 - \Omega_\theta/\gamma\omega_w). \tag{46}$$

Figure 14 shows the projection of the particle orbit in the transverse plane for $\gamma = 11$, $\varepsilon_t = -0.4$, $B_\theta = 11$ kG, $\omega_w = 6 \times 10^9\ \text{sec}^{-1}$, $r_0 = 100$ cm, $B_{z0} = 118$ G and $v_\theta \simeq c$. For these parameters, Eq. (43) gives a slow period $\tau_+ = 2\pi/\Omega_+ = 62$ nsec. For the same parameters the code gives $\tau_+ = 60$ nsec. In addition, Eq. (46) gives a displacement $\Delta r = 1.74$ cm, which is identical to the orbit displacement of Fig. 14.

Let us now return to discuss briefly the results of Fig. 10. For the parameters of the run, Eq. (42) gives $\gamma_+ \approx 121$ and $\gamma_- = 65$. When the γ of the particle reaches 65 i.e., at about 300 nsec, it becomes unstable and strikes the wall in one revolution.

In addition, at $t = 0$ the ratio $\Omega_\theta/\omega_w\gamma = 6.67$ and according to Eq. (46) the orbit displacement is negative. As γ increases, $\Omega_\theta/\gamma\omega_w$ is reduced and when $\Omega_\theta/\gamma\omega_w < 1$

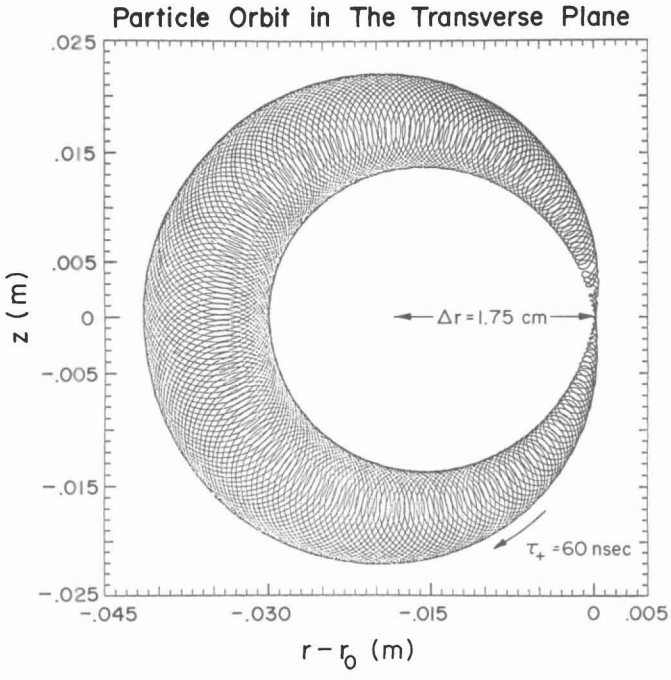

FIGURE 14 Particle orbit in the r, z plane for an initially mismatched beam and $\dot{\gamma} = 0$. The particle rotated around the equilibrium position four times with a period 60 nsec. The theory [Eq. (43)] predicts a period of 62 nsec and the nonlinear equations give similar orbits with a period of about 55 nsec.

the orbit displacement becomes positive. At $\gamma = 46.6$, $\Omega_\theta/\gamma\omega_w \approx 1$ and $\Delta r = 0$. According to Fig. 10b, this occurs at $t \approx 210$ nsec, which corresponds to $\gamma \approx 47$ (see Fig. 10c).

V. SELF FIELDS

An accurate self-consistent determination of self fields of a high-current electron ring confined in a rebatron is difficult, because the minor cross section of the ring has, in general, a complex shape that varies along the toroidal direction.

Since we are interested in the macroscopic motion of the ring and therefore on the self fields that act on the ring centroid, we assume that the ring has a circular cross section and its particle density is uniform. Neglecting toroidal corrections, the fields at the center of the beam, which is located at the distance $(r - r_0)$ and z from the minor axis are[18,26]

$$E_r^s = -2\pi |e| n_0 r_0 \frac{r_b^2}{a^2} \frac{(r - r_0)}{r_0} \tag{47}$$

$$E_z^s = -2\pi |e| n_0 r_0 \frac{r_b^2}{a^2} \frac{z}{r_0}, \tag{48}$$

$$B_r^s = 2\pi |e| n_0 \beta_0 r_0 \frac{r_b^2}{a^2} \frac{z}{r_0}, \tag{49}$$

and

$$B_z^s = 2\pi\,|e|\,n_0\beta_0 r_0\,\frac{r_b^2}{a^2}\,\frac{(r-r_0)}{r_0}, \tag{50}$$

where n_0 is the particle density, r_b the beam radius and a the minor radius of the perfectly conducting torus.

When $\dot{\gamma}=0$, $n=\frac{1}{2}$ and the beam energy is matched to the vertical field, the equation describing the beam centroid motion in the transverse rotating plane is given by

$$\ddot{\hat{\psi}} + \hat{f}_1\hat{\psi} + f_3\hat{\psi}^* - \mathrm{i}f_2\dot{\hat{\psi}} = \lambda^2 e^{\mathrm{i}\omega_w t/2}, \tag{51}$$

where f_2 and f_3 have been defined under Eq. (38) and

$$\hat{f}_1 = \hat{\omega}_\perp^2 - \left(\frac{\omega_w}{2}\right)^2 + \frac{\omega_w}{2}\frac{\Omega_\theta}{\gamma}, \tag{52}$$

where

$$\hat{\omega}_\perp^2 = \frac{v_\theta^2}{2r_0^2} - \frac{\omega_b^2}{2\gamma^3}\left(\frac{r_b}{a}\right)^2, \tag{53}$$

and $\omega_b^2 = 4\pi e^2 n_0/m$.

The solution of Eq. (51) when $\lambda^2=0$ is $\hat{\psi}=\sum_i \hat{\psi}_{0i}e^{\mathrm{i}\omega_i t}$, where

$$\omega_\pm^2 = \frac{1}{4}\left(\omega_w - \frac{\Omega_\theta}{\gamma}\right)^2 + \left(\frac{\Omega_\theta^2}{4\gamma^2} + \hat{\omega}_\perp^2\right) \pm \left[\left(\omega_w - \frac{\Omega_\theta}{\gamma}\right)^2\left(\frac{\Omega_\theta^2}{4\gamma^2} + \hat{\omega}_\perp^2\right) + \frac{\omega_0^2\omega_w^2}{4}\right]^{1/2}. \tag{54}$$

The orbits are stable provided

$$\frac{\Omega_\theta^2}{4\gamma^2} + \hat{\omega}_\perp^2 \geqslant 0, \tag{55}$$

and

$$\left[\hat{\omega}_\perp^2 - \left(\frac{\omega_2}{2}\right)^2 + \frac{\omega_w}{2}\frac{\Omega_\theta}{\gamma}\right]^2 - \frac{\omega_0^2\omega_w^2}{4} \geqslant 0. \tag{56}$$

Equation (56) can be written as

$$\hat{\mu} = \hat{\omega}_\perp^4 + 2\hat{\omega}_\perp^2\left(\frac{\omega_\omega}{2}\right)\left(\frac{\Omega_\theta}{\gamma} - \frac{\omega_w}{2}\right) + \left(\frac{\omega_w}{2}\right)^2\left[\left(\frac{\Omega_\theta}{\gamma} - \frac{\omega_w}{2}\right)^2 - \omega_0^2\right] \geqslant 0, \tag{57}$$

and its roots are given by

$$\frac{\hat{\omega}_{\perp\pm}^2}{(\omega_w/2)} = -\left[\left(\frac{\Omega_\theta}{\gamma} - \frac{\omega_w}{2}\right) \mp \omega_0\right]. \tag{58}$$

Substituting Eq. (42) into Eq. (58), we obtained the relation

$$\hat{\omega}_{\perp\pm}^2 = \left(\frac{\omega_w}{2}\right)^2\left(1 - \frac{\gamma_\pm}{\gamma}\right). \tag{59}$$

Note that when $\omega_w > 0$, $\gamma_+ > \gamma_-$ for either sign of Ω_θ. We have studied the stability of the macroscopic beam motion under various conditions. The most interesting

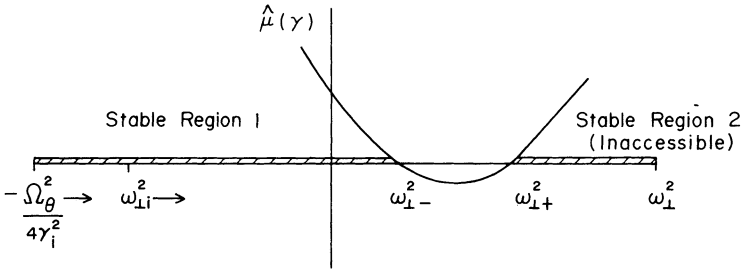

FIGURE 15 Plot of $\hat{\mu}(\gamma)$ of Eq. (57) as a function of $\hat{\omega}_\perp^2$. If the system is stable at $t=0$, it will remain stable for any γ that exceeds the initial γ.

case occurs when $\gamma > \gamma_+$. For this case the two roots $\hat{\omega}_{\perp\pm}^2$ are positive and $\hat{\omega}_{\perp+}^2 > \hat{\omega}_{\perp-}^2 > 0$, as shown in Fig. 15.

In region 1 of Fig. 15 the macroscopic beam motion is stable provided that

$$\hat{\omega}_{\perp-}^2 \geqslant \hat{\omega}_\perp^2 \geqslant -\frac{\Omega_\theta^2}{4\gamma^2}. \tag{60}$$

Substituting $\hat{\omega}_\perp^2$ from Eq. (53) and $\hat{\omega}_{\perp-}^2$ from Eq. (59) into the left inequality of Eq. (60), we find that

$$\left(\frac{\gamma}{\gamma_0}\right)^2\left(\frac{\gamma}{\gamma_0}-\frac{\gamma_+}{\gamma_0}\right)+\frac{1}{2\alpha^2 r_0^2} \geqslant 0, \tag{61}$$

where

$$\gamma_0^3 = \left(\frac{\omega_b r_0 r_b}{v_\theta a}\right)^2. \tag{62}$$

Since $\gamma > \gamma_+$, the inequality in Eq. (61) and therefore the left inequality in Eq. (60) is always satisfied. The condition $\gamma > \gamma_+$ can also be written as

$$1 > \frac{2}{\omega_w}\left(\frac{\Omega_\theta}{\gamma}+|\omega_0|\right).$$

The right inequality in Eq. (60) can be written as

$$\left(\frac{\gamma}{\gamma_0}\right)^3+\zeta^2\left(\frac{\gamma}{\gamma_0}\right)-1 \geqslant 0, \tag{63}$$

where

$$\zeta^2 = \left(\frac{\Omega_\theta r_0}{\sqrt{2}v_\theta \gamma_0}\right)^2.$$

The cubic equation corresponding to the equal sign in Eq. (63) has a positive real root and a pair of complex conjugate roots. Notice that for $\gamma > \gamma_0$ the inequality in Eq. (63) is always true. For the parameters of interest $\zeta^3 \gg 1$. In this case, the positive real root is approximately equal to $1/\zeta^2$ and therefore Eq. (63) is valid for

all $\gamma > \gamma_i$, when the initial value of γ, i.e. γ_i satisfies the inequality

$$\gamma_i/\gamma_0 \geqslant 1/\zeta^2 \quad \text{or} \quad \nu/\gamma_i \leqslant \Omega_\theta^2 a^2/8c^2, \tag{64}$$

where ν is the Budker parameter.

Thus, when $\gamma > \gamma_+$ the macroscopic beam motion is stable provided that Eq. (64) is satisfied. This is a very lenient condition because for $a = 10$ cm, $B_\theta = 10$ kG, $\gamma = 7$, Eq. (64) gives $\nu \simeq 3{,}000$ or $I \simeq 50$ MA.

Under the same conditions, i.e. when $\gamma > \gamma_+$, the region 2 in Fig. 2 is inaccessible. The reason is that $v_\theta^2/2r_0^2$, which is the maximum positive value of $\omega_\perp^2$ is less than $\omega_{\perp+}^2$.

Finally, it should be noticed that Eqs. (36) and (37) have been solved under the assumption $|\omega_0\omega_w| \gg \delta\omega^2$ and therefore Eq. (64) is valid under the implicit assumption that $\omega_0 \neq 0$.

VI. CONCLUSIONS

We have carried out an extensive numerical and analytical investigation of the beam dynamics in a rebatron accelerator. Although the analytical work is based on simple linear approximations for the various fields, the two approaches give very similar results when these approximations are valid.

Our studies indicate that when self-field effects can be ignored, the normalized particle energy can be increased from $\gamma = 7$ to $\gamma \approx 70$, at constant betatron field before confinement is lost. This implies that the device has a bandwidth that approaches 1000%. This bandwidth can be further increased by increasing the current in the torsatron wires.

Even in the absence of space charge, there is a range of parameters [see Eq. (42)] for which the rebatron is unstable. However, this orbit instability can be easily avoided by a judicious choice of the various parameters.

As far as orbit stability is concerned, the maximum electron-beam current that can be confined in a rebatron accelerator is given by Eq. (60) and is impressively high. Therefore it is expected that the limiting beam current in a rebatron would be determined from collective instabilities and not from the macroscopic stability of beam orbits.

Although the bandwidth of rebatron accelerators is very high, the maximum energy that can be obtained by these devices, with time-independent magnetic fields, is rather limited. To achieve very high energies ($\gamma \geqslant 1000$), the betatron magnetic field should be replaced by a local vertical magnetic field that varies rapidly with time and approximately in synchronism with the beam energy. Such a fast vertical field can be generated by two coaxial cylindrical lines that carry current in opposite directions. The axes of these lines coincide with the major axis of the toroidal vessel and they are located symmetrically around the minor axis of the torus. These transmission lines change mainly the local vertical magnetic field, while the magnetic flux through the beam orbit remains approximately constant. The mismatch between the beam energy and the vertical field is alleviated by the

strong focusing field. The effect of the rapidly varying vertical magnetic field on the beam dynamics will be reported in a forthcoming publication.

REFERENCES

1. C. A. Kapetanakos and P. Sprangle, *Phys. Today*, V. 38, #2 (Feb 1985), p. 58.
2. C. A. Kapetanakos and P. Sprangle, NRL Memo Report No. 5259, 1984 AD-A142303.
3. E. T. Gerry and S. A. Mani, W. T. Schafer Associates Report No. DOE/ER-0176 (1983).
4. P. Sprangle and T. Coffey, *Phys. Today*, V. 36, #12 (Dec 1983).
5. D. Keefe, *Part Acc.* **11,** 187 (1981).
6. N. C. Christofilos, *et al., Rev. Sci. Instrum.* **35,** 886 (1964).
7. J. E. Leiss, N. J. Norris and M. A. Wilson, *Part. Acc.* **10,** 223 (1980).
8. T. J. Fessenden, *et al.*, Proc. of the Int. Top. Conf. on High-Power Electron and Ion Beam Research and Technology: Palaiseau, France, June 29-July 3, 1981, p. 813. AD-A057 218 Vol. I, AD A057 219 Vol. II, March 78, edition.
9. R. J. Briggs, *et al.*, Proc. 1981 Particle Accel. Conf.; *IEEE Trans. Nucl. Sci. NS-28* (June 1981), p. 3360.
10. A. I. Pavlovskii, *et al., Sov. Phys. Dokl.* **25,** 120 (1980).
11. K. R. Prestwich, *et al., IEEE Trans. on Nucl. Sci. NS-30*, 3155 (1983).
12. L. N. Kazanskii, A. V. Kisletsov and A. N. Lebedev, *Atomic Energy* **30,** 27 (1971).
13. M. Friedman, *Appl. Phys. Lett.* **41,** 419 (1982).
14. D. W. Kerst, *Nature* **157,** 90 (1946).
15. A. I. Pavlovskii, *et al., Sov. Phys. Tech. Phys.* **22,** 218 (1977).
16. P. Sprangle and C. A. Kapetanakos, *J. Appl. Phys.* **49,** 1 (1978).
17. N. Rostoker, *Comments on Plasma Physics*, Vol. 6, p. 91 (1980).
18. C. A. Kapetanakos, P. Sprangle, D. P. Chernin, S. J. Marsh and I. Haber, *Phys. Fluids* **26,** 1634 (1983).
19. C. W. Roberson, A. Mondelli and D. Chernin, *Phys. Rev. Lett.* **50,** 507 (1983).
20. L. Teng, Argonne Nat. Lab. Report No. ANLAB-55 (1959); G. Salardi, *et al., Nucl. Instr. and Methods* **59,** 152 (1968); R. M. Pearce, *Nucl. Instr. and Methods* **83,** 101 (1970); R. L. Gluckstern, *Proc. Kinear Accel. Conf.*, 1979, p. 245.
21. A. A. Mondelli and C. W. Roberson, *Particle Accelerators* **15,** 221 (1984).
22. P. Sprangle and C. A. Kapetanakos, NRL Memo Report No. 5458 (1984); *Part. Accel.* (1985).
23. P. A. Politzer, MIT Report No. 77-1 (1977).
24. R. E. Potok, H. Becker, L. Bromberg, D. Cohn, N. Diatchenko, P. B. Roemer and J. E. C. Williams, MIT Report PFC/RR-82-10 (1982).
25. I. S. Danilkin, in *Stellarators*, Proc. of the P.N. Lebeder Inst. (Consultants Bureau, N.Y. 1974) Vol. 65, p. 23. [Note: We have rederived the toroidal correction and found that two signs in the expression for the potential are different than those given by Danilkin in his Eqs. (24) and (26)].
26. P. Sprangle, C. A. Kapetanakos and S. J. Marsh, NRL Memo Report No. 4666 (1981), (AD-A108359).